Demultiplexing sound in stacked valley-Hall topological insulators

Wei Xiong,[1] Penglin Gao [©],[2] Zhiwang Zhang [©],[1,*] Zichong Yue,[1] Haixiao Zhang [©],[1] Ying Cheng,[1,3,†]
Xiaojun Liu,[1,3,‡] and Johan Christensen [©][2,§]

[1]*Department of Physics, MOE Key Laboratory of Modern Acoustics, Collaborative Innovation Center of Advanced Microstructures,
Nanjing University, Nanjing 210093, China*
[2]*Department of Physics, Universidad Carlos III de Madrid, ES-28916 Leganés, Madrid, Spain*
[3]*State Key Laboratory of Acoustics, Institute of Acoustics, Chinese Academy of Sciences, Beijing 100190, China*

Demultiplexing is used to connect data or signals from one single channel stream to multiple destinations. The streams may be additionally divided through their frequency, polarizations, angular momentum, etc. Here, we show how one is able to demultiplex sound waves at different physical positions and frequency components by employing stacked valley-Hall topological insulators made of merged triangular rigid scatterers. By tuning their two relative angles, we are able to break or restore the underlying lattice symmetry within two topologically independent band gaps. Thus, we experimentally stacked various individually tuned valley-Hall insulators to enable spectrally specific radiated sound to be routed to a particular destination via scattering-immune valley-projected edge states. We foresee that these findings will advance further studies in condensed matter physics, classical wave physics, but also in technological areas of communication by capitalizing on unconventional valley-Hall physics.

I. INTRODUCTION

Valley-Hall effects reside at the frontier in a very active arena of condensed matter physics [1–3], where associated valley-Hall topological insulators (VHTIs) are considered as a particular popular member among exotic structures, capable of confining states owing to their underlying topology. Robust valley transport requires no breaking of the time-reversal symmetry, but remains resilient only under certain symmetry-preserving defects or imperfections [4–9]. The topology is usually defined across the entire band within the Brillouin zone (BZ), however, concerning valley-contrasting physics, a nonzero topological charge called the valley Chern number, is found to be localized around the valleys at the corners of the BZ. The valleys, i.e., the band extrema of the gapped Dirac cones, are formed by lifting the inversion symmetry of the lattice and carry opposite topological charges, which implies that their corresponding vortex states have differing chiralities that can be harnessed to launch one-way valley transport, beam splitting, and refraction control of outcoupled valley edge excitations [4–7,10].

Phononic media, i.e., sonic and elastic crystals, have proven to be versatile platforms to emulate with sound and vibrations the valley-Hall related phenomena and effects. However, similar to their metamaterial counterpart [11], most of their counterintuitive characteristics are only found within a single and often narrow band of frequencies [12–21]. Here,

we merge two C_3-symmetric scatterers as the elementary unit of an artificial triangular sonic crystal (SC); through rotational tuning of this unique scatterer, one is able to engineer spectrally independent band inversion of dissimilar valley-Hall phases across different topological band gaps. This approach enables us to study yet unseen valley physics as we deliberately fabricate such an arrangement by stacking various VHTIs to facilitate spatially and spectrally separated sensing of acoustic audio signals. Particularly, in the presence of superimposed background noise, we experimentally show how two parallel signals can be efficiently demultiplexed to their in-gap topological components, which should find important use in the frequency-selective sonic separation of signals.

II. RESULTS AND DISCUSSION

A. Designing the stacked acoustic valley-Hall topological insulators

We begin by constructing various SCs by merging two identical C_3-symmetric rigid scatterers with the rotation angles θ_1 and θ_2, from which we can harvest various topological valley-Hall phases that are induced by individually broken or preserved lattice symmetries as displayed through the six SCs (A–F) in Fig. 1(a). We emphasize, in comparison to the regular VHTI composed of a single scatterer that may feature dual topological band gaps [22,23], the present design comprising two merged C_3 scatterers allows for the independent creation and control of valley properties across two distinct band gaps [24]. The band diagrams of the aforementioned six topologies are computed as shown in Figs. 1(b) and 1(c). Two points should be noted here: (i) The opening and closing of two Dirac cones at the low- (LF) and high-frequency (HF)

---

*zhangzhiwang@nju.edu.cn
†chengying@nju.edu.cn
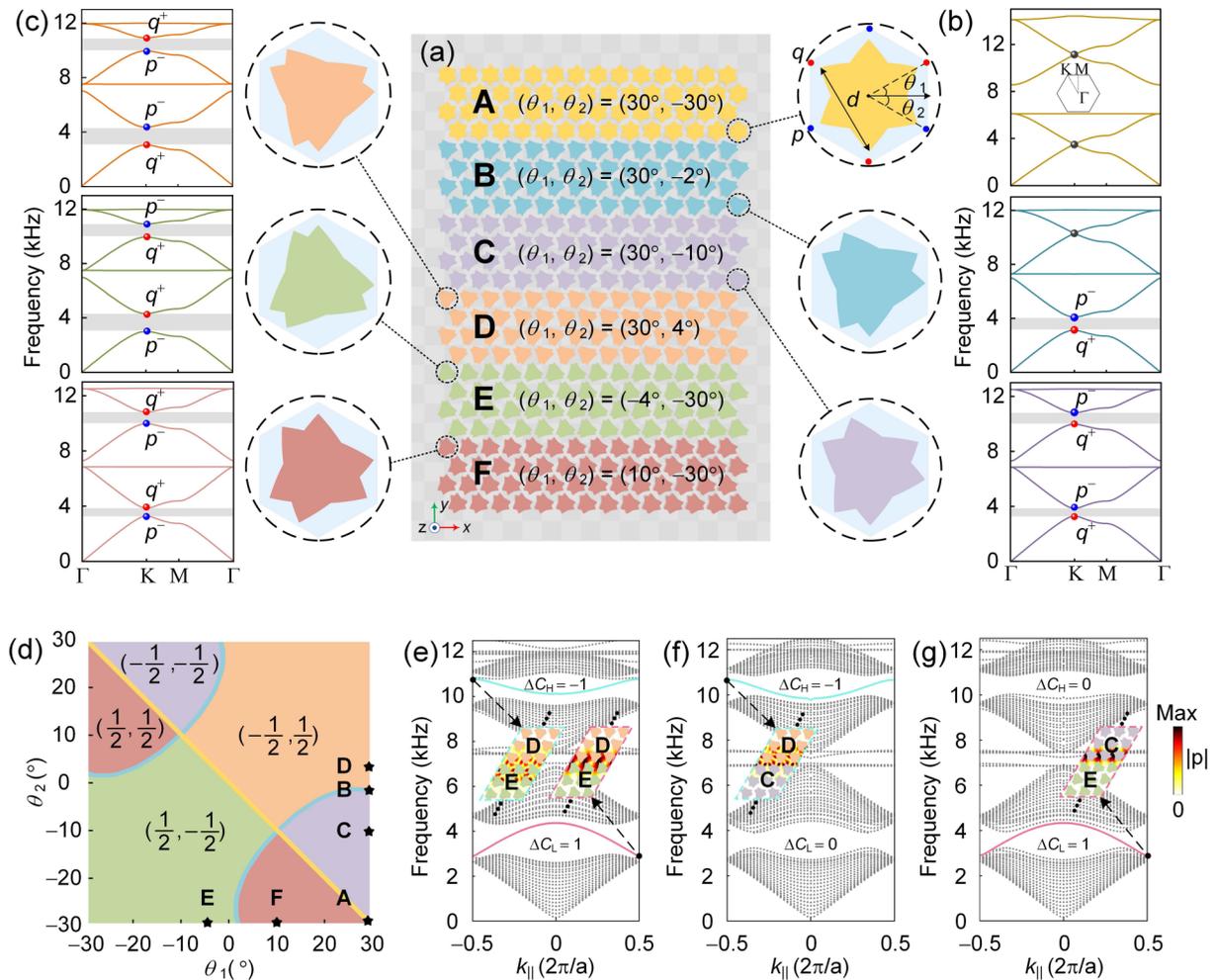‡liuxiaojun@nju.edu.cn
§johan.christensen@gmail.com

FIG. 1. Stacked valley-Hall topological insulators. (a) Two C_3-symmetric scatterers are merged with rotation angles θ_1 and θ_2 to form a variety of highly tunable primitive cells. Thus, we construct six SCs of different topologies that are labeled A–F, and compute their corresponding band diagrams shown in (b) and (c). The shaded regions mark the complete band gaps whereas the black, red, and blue dots at the K point label the Dirac cone, q^+ and p^- modes, respectively. (d) By varying θ_1 and θ_2 we compute a phase diagram of topological band gaps across two spectral windows. We distinguish between four colored zones with respective pairs of quantized topological invariants, which are separated by phase boundaries where the states degenerate. The stars on the diagram indicate the phase locations where the six individual SCs can be found. (e)–(g) Thus, we construct three different topological interfaces with different high- and low-frequency valley-Chern indices, whose computed projected edge dispersion relations are shown together with their pressure field maps.

regions can be controlled independently. For SC-A with $\theta = (\theta_1, \theta_2) = (30°, -30°)$ [the first panel in Fig. 1(b)], the C_{3v} symmetry is still preserved and single Dirac cones in both bands can be clearly seen at the K point. After rotating the merged scatterers to $\theta = (30°, -2°)$ [the second panel in Fig. 1(b)], the Dirac cone of the LF band is opened to form a complete gap, unlike the HF one that still remains degenerated. The remaining SCs (C–F) display that both Dirac cones are gapped at their respective angular rotations. (ii) Nevertheless, although we achieve complete band gaps for these four cases, the mode properties and the topological valley-Hall phases have undergone distinct changes. The colored dots p^- and q^+ at the K points of the band diagrams represent the valley modes with clockwise and counterclockwise vortices, respectively [24]. The topological valley-Chern index can be derived from the eigenfrequencies of these two distinct vortex modes through the equation $C^K = \text{sgn}(m)/2$,

where $m = (\omega_{q^+} - \omega_{p^-})/2v_D^2$ is the effective mass term in the reduced effective Dirac Hamiltonian [12]. Since we have two topological band gaps, we define a dual-band valley-Chern index $C^K = (C_L^K, C_H^K)$ with C_L^K / C_H^K for the LF/HF bands. The Wilson loop characterization of the valley-Hall phases [25] is discussed elsewhere [24]. In Fig. 1(d) we display the topological phase diagram in two angular degrees of freedom space respecting the C_3 symmetry of the scatterer. Four phase regions of different topological valley indices are separated by one golden line and two aqua curves. The golden line represents the phase boundaries where both the LF and HF band gaps are closed (as for the SC-A), and the aqua curves indicate the absence of the HF band gap but the existence of the LF one (as for the SC-B). Calculated nonzero topological valley-Chern indices in the remaining four regions are marked correspondingly and contain omnidirectional band gaps in both the LF and HF bands. According
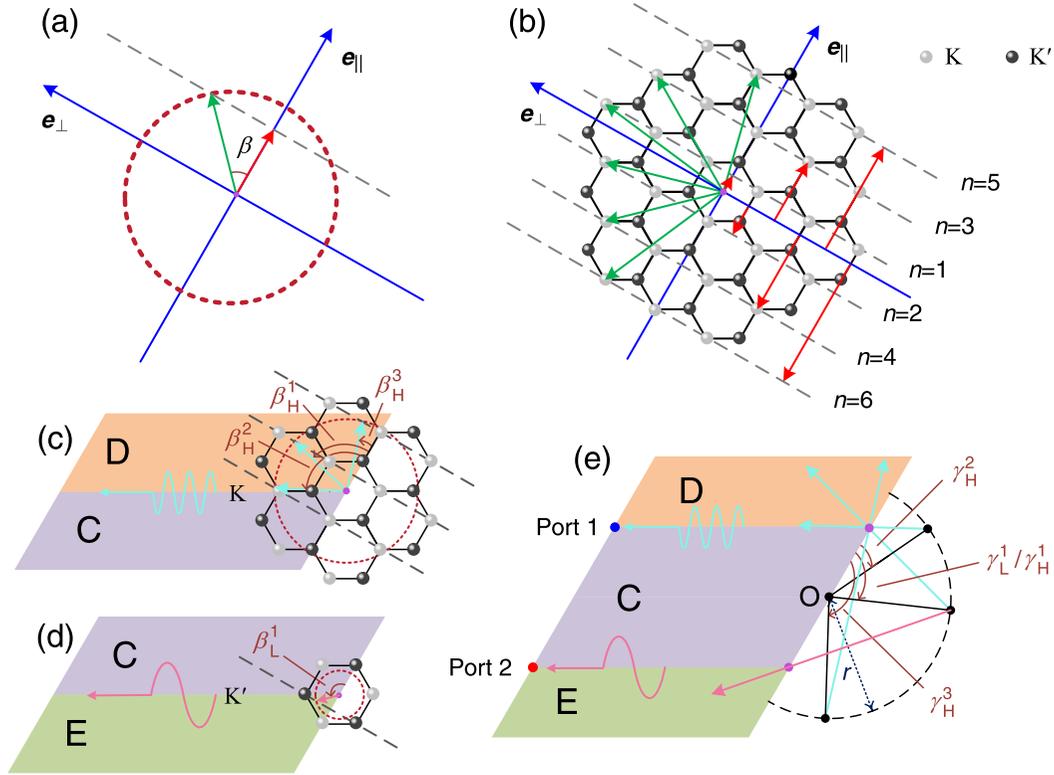
FIG. 2. Momentum matching of topological edge states with radiated sound. Projection of (a) wave vectors in free space and (b) the *K* valley states of the lattice onto the structure termination. (c) HF edge states projected along the DC interface, and likewise in (d) for LF edge states along the CE interface. (e) Momentum matching for the DCE stack comprising the dual channel.

to the bulk-boundary correspondence [26], the topological valley-projected edge states (VPESs) are protected along the domain wall between two regions of opposite valley-Hall phases [12,14]. Owing to the additionally introduced degree of freedom, VPESs can be individually controlled within their hosting band gap through arranging SCs as desired. Among an array of VHTI stacking possibilities as shown Fig. 1(a), we are entitled to deliberately acquire a spectral selection of VPESs across two band gaps. Consequently, the rule for the existence or absence of edge states is set by the difference of the valley-Chern index across the chosen interface in both band gaps. Figures 1(e)–1(g) illustrate three kinds of stacked frequency-selective VHTIs. In Fig. 1(e), the domain wall between SC-D and SC-E preserves the difference of the dual-band valley-Chern indices with $\Delta C_L^K = 1$, $\Delta C_H^K = -1$. Consequently, VPESs should appear in the first (second) band gap comprising a positive (negative) group velocity dispersion, which can be further manipulated through cunningly contrived stacking [24]. Next, if we keep the structure above the domain wall unchanged (SC-D) but replace the lower one with SC-C of the stack, one obtains topological indices according to $\Delta C_L^K = 0$ and $\Delta C_H^K = -1$, which renders the LF band gapped but the HF unchanged [compared to Fig. 1(e)] as shown in Fig. 1(f). Lastly, with the specific CE VHTI stack, we are able to acquire a frequency inverted scenario as shown in Fig. 1(g). Here, according to the dual-band indices, the stack sustains only a VPES in the LF band. Conclusively, by carefully rotating two merged C_3 sound hard scatterers, one is able to engineer VHTI stacks with frequency-selective

and topologically independent interface states across two bands. This finding is in stark contrast to previous approaches where states within different topological bands appear and vanish concurrently. Based on this salient feature, a tunable topological acoustic frequency-selective beam splitter can be constructed [24].

B. Valley-momentum matching process

The reception of airborne sound in the stacked VHTI adheres to valley-projected physics, but requires additionally that the incoming acoustic radiation momentum **k** matches well to the VPES momentum **K** that ultimately carries sound along the structure. Hence, free-space sound has to be projected onto the stack termination, i.e., parallel to the unit vector $\mathbf{e}_\parallel$ [Fig. 2(a)] and likewise for the state that is projected from the *K* valley [Fig. 2(b)], where *n* defines the multiple orders, at which the latter can be made possible as indicated by the gray dashed lines. Without loss of generality, the wave vector matching condition $\mathbf{k} \cdot \mathbf{e}_\parallel = \mathbf{K} \cdot \mathbf{e}_\parallel$ [7,27] can be rewritten as

$$\left[\frac{2\pi f}{c} \cos(\beta) \right] |\mathbf{e}_\parallel| = \left(M \times \frac{2}{3} \times \frac{2\pi}{a} \right) |\mathbf{e}_\parallel|, \quad (1)$$

where $M = 1/2 \times \left(\frac{3n-1}{2} - \frac{(-1)^n+1}{4} \right) \times (-1)^{(n+1)}$ is a parameter related to *n*, *f* represents the working frequency, *c* is the sound velocity, *a* is the lattice constant, and β denotes the theoretical reception angle. The DC and CE VHTI stacks we computed in Fig. 1 will be further characterized, in that
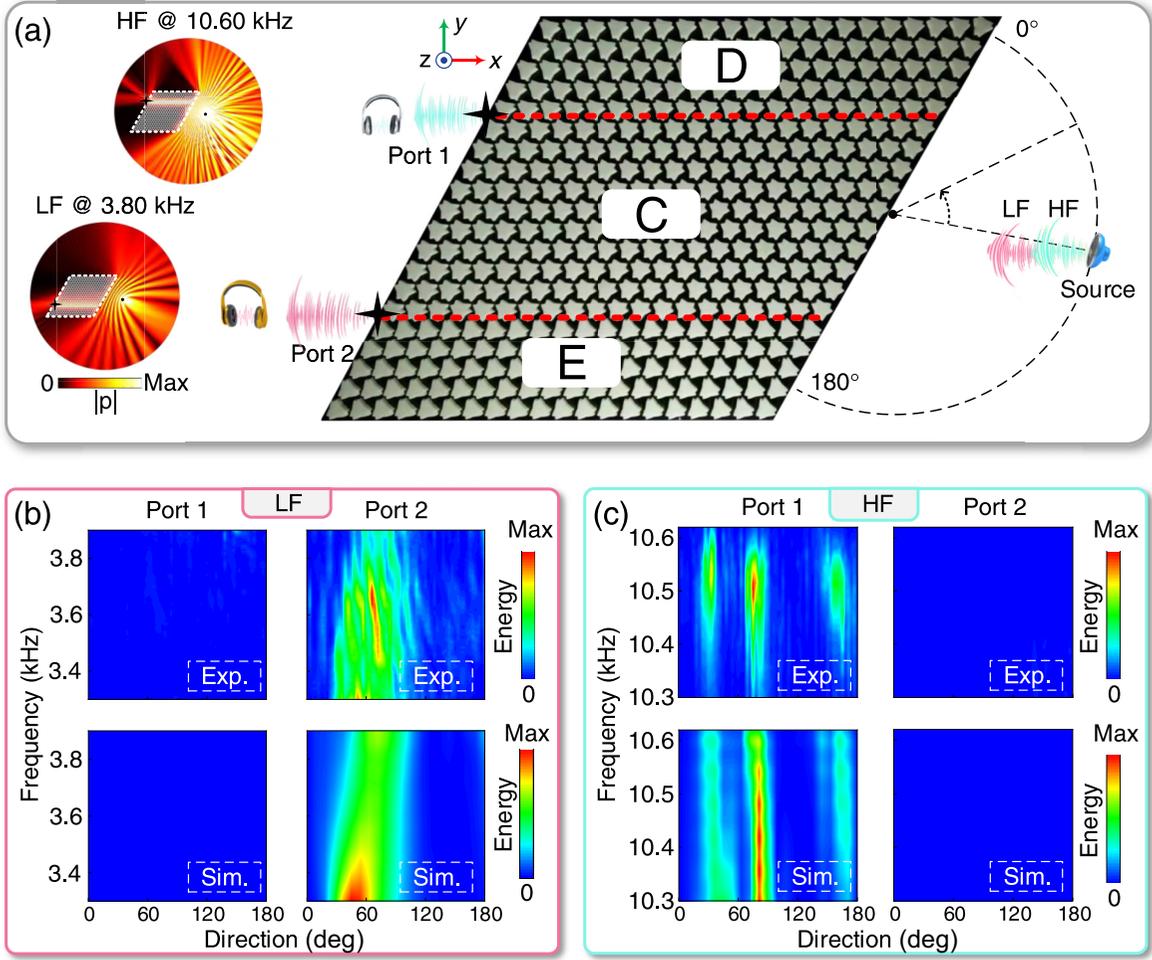
FIG. 3. Space and frequency separated reception of sound. (a) Photograph of the fabricated stack (without the top cover). Insets: Simulated distributions of the absolute pressure fields in the LF (left bottom, $f = 3.80$ kHz) and the HF band (left top, $f = 10.60$ kHz). Domain walls are highlighted by red dashed lines. The black dashed semicircle represents the position of the point source during the angular scan, whereas at port 1 and port 2 (black stars) of the termination, the receiver signals are detected. (b) Experimentally measured (upper two panels) and simulated (bottom two panels) energy at port 1 and port 2 by scanning the incident angle of the source across the first topological band (LF). (c) Same as (b), but for the second band (HF).

we analytically calculate their reception (sensing) angles, at their respective frequencies. By applying Eq. (1), the wave vector matching processes in these two cases are illustrated in Figs. 2(c) and 2(d). Three theoretical sensing angles β_H^1, β_H^2, and β_H^3 in the HF band of the DC stack and one angle β_L^1 in the LF band of the CE stack are obtained:

$$\beta_H^1 = \arccos\left(\frac{c}{3af}\right), \quad \beta_H^2 = \pi - \arccos\left(\frac{2c}{3af}\right),$$

$$\beta_H^3 = \arccos\left(\frac{4c}{3af}\right), \quad \text{for } f \geqslant 10.53 \text{ kHz},$$

$$\beta_L^1 = \pi - \arccos\left(\frac{c}{3af}\right). \tag{2}$$

Eventually, a DCE stack is considered to form a unit capable of hosting the two spectrally independent VPESs whose properties were discussed in the former. As Fig. 2(e) illustrates, we delineate a new point of origin O that defines the central point

from which we draw a detection radius with $r = 37.77$ cm. The new analytical sensing angles γ_i^n, with $i = \text{L, H}$, can be retrieved from β_i^n according to the relations

$$\gamma_H^n = \arccos\left(\frac{25a^2 + r^2 - D_H^n}{10ar}\right),$$

$$\gamma_L^n = \pi - \arccos\left(\frac{25a^2 + r^2 - D_L^n}{10ar}\right),$$

$$D_i^n = 1/4\left[-B_i^n + \sqrt{(B_i^n)^2 - 4(25a^2 - r^2)}\right]^2, \quad i = \text{L, H},$$
$$\tag{3}$$

where $B_H^n = 5a\cos(\beta_H^n - \frac{2\pi}{3}) + 5\sqrt{3}a\sin(\beta_H^n - \frac{2\pi}{3})$ and $B_L^n = -[5a\cos(\beta_L^n - \frac{2\pi}{3}) + 5\sqrt{3}a\sin(\beta_L^n - \frac{2\pi}{3})]$. For the working frequencies $f_{LF} = 3.80$ kHz and $f_{HF} = 10.60$ kHz, the theoretical sensing angles become $\gamma_H^1 = 70.6°$, $\gamma_H^2 = 30.3°$, and $\gamma_H^3 = 170.2°$ in the HF and $\gamma_L^1 = 70.6°$ in the LF band.
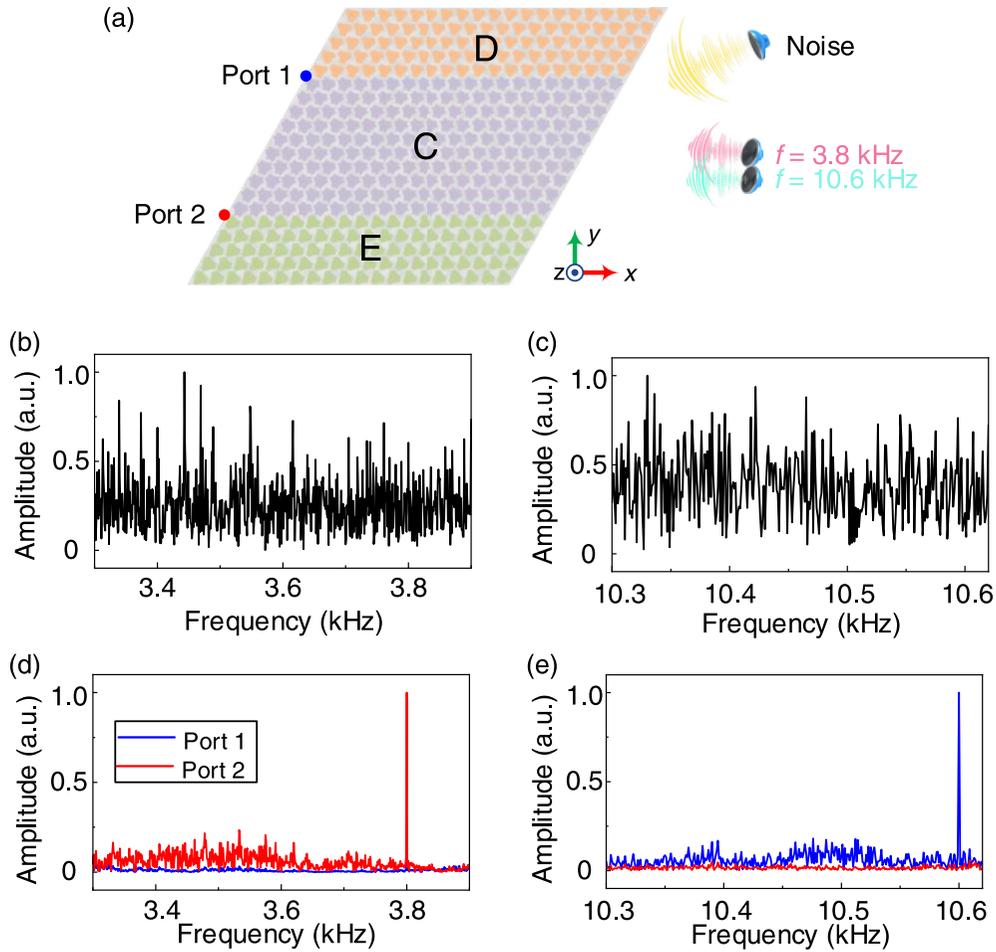
FIG. 4. Demultiplexing topological sound in the presence of interfering noise. (a) A DCE valley-Hall stack is irradiated by two weak sources, each set to emit sound at $f = 3.80$ kHz and $f = 10.60$ kHz and placed at 70.6° with a distance of 37.77 cm from the termination center of the device. At the same distance, but at an angle of 12°, another source is situated that emits strong broadband white interference noise to mask the desired signal. Frequency spectra of the signals measured in free space without the topological device in the (b) lower- and (c) higher-frequency range. (d), (e) Same as (b), (c) but measured at port 1 (blue curve) and port 2 (red curve) when using the stacked device.

C. Topological sound demultiplexing

Having derived the discrete angles at which the DCE VHTI stack efficiently is able to detect sound via two independent valley paths, we now construct such a system based on the foregoing discussion in Fig. 2(e). Figure 3(a) shows a photograph of the fabricated sample comprising a stack of the three SCs, i.e., the DCE VHTI. With respect to the phase-matching condition at the stack termination, we displace a single acoustic source angularly at a constant distance of 37.77 cm from 0° to 180°, and frequency sweep separately within the topological band gaps of interests, i.e., the LF (3.30–3.90 kHz) and the HF band (10.30–10.62 kHz). Once the radiated sound is appropriately collected via the respective VPESs, its energy is probed at the ports at the far side of the DCE stack [24]. The bottom panels of Figs. 3(b) and 3(c) show the simulated results in the LF and HF band gaps, respectively. Here, the data show that within the first gap, acoustic signals are entirely suppressed from port 1, but compare fairly well to our theoretical predictions (70.6° at $f_{LF} = 3.80$ kHz) for sound detected at port 2. On the other hand, according to the theo-

retical predictions at $f_{HF} = 10.60$ kHz, we now sweep across the HF topological band gap and detect three distinct peaks at the angular positions: 30.3°, 70.6°, and 170.2°. We find that at those positions, the source is capable of exciting the VPESs along the upper interface towards port 1, whereas now signals are entirely undetectable at port 2. The corresponding experimentally measured results are depicted in the top panels of Figs. 3(b) and 3(c), which show excellent agreement with the theoretical and simulated results.

The aforementioned dual-channel topological sensor plays a pivotal role in picking up and distinguishing signals from specific directions. With respect to the phase-matching conditions, we have a set of discrete angular positions to make topological spectral separation possible. According to the theory, the angles $\gamma_L^1 = \gamma_H^1$ in our DCE stack, which implies that acoustic signals with frequency components within either topological band gaps can be efficiently demultiplexed when emanating from a position at $\gamma_{L,H}^1 = 70.6°$. Hence, at the same distance as before, we place two sources at their nearest proximity, each insonifying the DCE VHTI as depicted in Fig. 4(a)

at their indicated in-gap frequency. Moreover, to challenge the topological demultiplexer further, we mimic traffic noise by a broadband white-noise source (spanning across both band gaps) that is placed at the angular position of $12°$. The intent is to mask the two signals of interest entirely as the free-space measured amplitude spectra in Figs. 4(b) and 4(c) display. Here, it is seen how the weak signals within each topological band gap are completely drowned in noise. Nevertheless, once the topological DCE stack is utilized, not only are we able to spatially and spectrally separate sound at different destinations, the interference noise is greatly suppressed while the signal is fully perceived only at port 2 ($f = 3.80$ kHz) [port 1 ($f = 10.60$ kHz)] as measurements show in Fig. 4(d) [Fig. 4(e)].

III. CONCLUSIONS

By merging two C_3-symmetric rigid scatterers, we engineered an alternate tunable degree of freedom through rotation, which entails spectrally separated valley-Hall phases of independent band topology. This approach allows us to embark on other topological avenues where the stacking of differing valley-Hall topological insulators implies individual valley-Hall phases across two band gaps, comprising unconventional band inversion processes and degeneracies. These characteristics in stacked topological insulators warrant the demultiplexing of acoustic signals even in the presence of pronounced background noise as coming from traffic. Thus, we showed how the spectral and spatial separation of signals is possible owing to this valley-Hall band topology, which should find immediate interest to enhance the channel capacity and communication quality in sound reception and manipulation.

[1] A. Rycerz, J. Tworzydło, and C. Beenakker, Nat. Phys. **3**, 172 (2007).

[2] D. Xiao, W. Yao, and Q. Niu, Phys. Rev. Lett. **99**, 236809 (2007).

[3] F. Zhang, A. H. MacDonald, and E. J. Mele, Proc. Natl. Acad. Sci. USA **110**, 10546 (2013).

[4] T. Ma and G. Shvets, New J. Phys. **18**, 025012 (2016).

[5] J.-W. Dong, X.-D. Chen, H. Zhu, Y. Wang, and X. Zhang, Nat. Mater. **16**, 298 (2017).

[6] J. Noh, S. Huang, K. P. Chen, and M. C. Rechtsman, Phys. Rev. Lett. **120**, 063902 (2018).

[7] F. Gao, H. Xue, Z. Yang, K. Lai, Y. Yu, X. Lin, Y. Chong, G. Shvets, and B. Zhang, Nat. Phys. **14**, 140 (2018).

[8] B. Orazbayev and R. Fleury, Nanophotonics **8**, 1433 (2019).

[9] G.-J. Tang, X.-D. Chen, F.-L. Shi, J.-W. Liu, M. Chen, and J.-W. Dong, Phys. Rev. B **102**, 174202 (2020).

[10] B. Hu, Z. Zhang, H. Zhang, L. Zheng, W. Xiong, Z. Yue, X. Wang, J. Xu, Y. Cheng, X. Liu, and J. Christensen, Nature **597**, 655 (2021).

[11] S. Cummer, J. Christensen, and A. Alú, Nat. Rev. Mater. **1**, 16001 (2016).

[12] J. Lu, C. Qiu, L. Ye, X. Fan, M. Ke, F. Zhang, and Z. Liu, Nat. Phys. **13**, 369 (2017).

[13] B.-Z. Xia, S.-J. Zheng, T.-T. Liu, J.-R. Jiao, N. Chen, H.-Q. Dai, D.-J. Yu, and J. Liu, Phys. Rev. B **97**, 155124 (2018).

[14] Z. Zhang, Y. Tian, Y. Cheng, Q. Wei, X. Liu, and J. Christensen, Phys. Rev. Appl. **9**, 034032 (2018).

[15] Z. Tian, C. Shen, J. Li, E. Reit, H. Bachman, J. E. Socolar, S. A. Cummer, and T. J. Huang, Nat. Commun. **11**, 762 (2020).

[16] J. Vila, R. K. Pal, and M. Ruzzene, Phys. Rev. B **96**, 134307 (2017).

[17] H. Zhu, T.-W. Liu, and F. Semperlotti, Phys. Rev. B **97**, 174301 (2018).

[18] M. Miniaci, R. K. Pal, R. Manna, and M. Ruzzene, Phys. Rev. B **100**, 024304 (2019).

[19] Q. Zhang, Y. Chen, K. Zhang, and G. Hu, Extreme Mech. Lett. **28**, 76 (2019).

[20] X. Zhang, M. Xiao, Y. Cheng, M.-H. Lu, and J. Christensen, Commun. Phys. **1**, 97 (2018).

[21] Z. Zhang, H. Long, C. Liu, C. Shao, Y. Cheng, X. Liu, and J. Christensen, Adv. Mater. **31**, 1904682 (2019).

[22] Z. Zhang, Y. Gu, H. Long, Y. Cheng, X. Liu, and J. Christensen, Research **2019**, 5385763 (2019).

[23] D. Jia, Y. Ge, H. Xue, S.-Q. Yuan, H.-X. Sun, Y. Yang, X.-J. Liu, and B. Zhang, Phys. Rev. B **103**, 144309 (2021).

[24] See Supplemental Material at http://link.aps.org/supplemental/10.1103/PhysRevB.104.224108 for calculations of the valley-Chern index, altering valley-projected edge states, and measured frequency-selective beam splitting.

[25] H.-X. Wang, G.-Y. Guo, and J.-H. Jiang, New J. Phys. **21**, 093029 (2019).

[26] M. Ezawa, Phys. Rev. B **88**, 161406(R) (2013).

[27] Z. Zhang, Y. Tian, Y. Wang, S. Gao, Y. Cheng, X. Liu, and J. Christensen, Adv. Mater. **30**, 1803229 (2018).